BMC Medical Imaging

RESEARCH

Open Access

Consensus clustering based on CT radiomics has potential for risk stratification of patients with clinical T1 stage lung adenocarcinoma

Hao Dong[1,2†], Yang Li[3†], Lingli Zhao[1†], Lekang Yin[4], Xiaojun Guan[1], Xiaodan Ye[4*] and Xiaojun Xu[1*]

Abstract

Background This study aimed to clinically risk-classify patients with clinical stage T1 LUAD based on consensus clustering of CT radiomics to help clinics provide personalized treatment strategies for patients with early stage LUAD.

Materials Clinical, pathological and CT imaging data of patients who underwent surgical resection and pathologically confirmed lung adenocarcinoma from September 2018 to May 2021 were retrospectively analysed. The clinical and pathological information included age, gender, smoking history, tumor location, pathological subtype, infiltration level, lymph node metastasis (LNM), visceral pleural infiltration (VPI), lymphovascular invasion (LVI), spread through air space (STAS), Ki-67 proliferation index, and gene mutation information. Unsupervised consensus clustering analysis was performed based on the radiomic features of CT images to determine the optimal cluster values and evaluate the effect of consensus clustering. Patients were grouped according to the consensus clustering results, and compared with the histopathological characteristics of the tumors, genomic information and subgroup analyses were performed in invasive adenocarcinomas and sub-solid lesions.

Results Totally 497 cases were determined to be classified into 2 clusters (optimal), with 258 (51.9%) cases in cluster 1 and 239 (48.1%) cases in cluster 2. There were statistically significant differences between cluster 1 and cluster 2 in micropapillary component, solid component, STAS, and Ki-67 proliferation index ($p < 0.001$), as well as statistically significant differences in LNM and VPI ($p = 0.031$ and 0.012 respectively). Additionally, micropapillary component, solid component, STAS, and Ki-67 proliferation index were also statistically different in subgroup analyses of invasive adenocarcinomas and sub-solid foci ($p < 0.05$). The clusters 1 and 2 were statistically different only in *HER2* mutations ($p < 0.001$).

Conclusion Consensus clustering based on CT radiomics can identify the associations of radiomic features between pathological risk factors and genomic features in clinical stage T1 lung adenocarcinoma, which can help clinical risk stratification of stage T1 lung adenocarcinoma patients.

†Hao Dong, Yang Li and Lingli Zhao contributed equally to this work.

*Correspondence:
Xiaodan Ye
yuanyxd@163.com
Xiaojun Xu
xxjmailbox@zju.edu.cn

Full list of author information is available at the end of the article

Clinical trial number Not applicable.

Keywords Lung adenocarcinoma (LUAD), Risk stratification, Consensus clustering, Radiomics

Introduction

Latest data reveals that lung cancer has been the foremost contributor to cancer-associated deaths worldwide, comprising 18.0% of all cancer deaths [1]. Non-small cell lung cancer (NSCLC) constitutes 85% of all lung cancer types, with lung adenocarcinoma (LUAD) emerging as the predominant histologic type [2]. Surgical resection is the primary and favored approach for addressing early-stage lung cancer [3]. The sublobar resection (segmentectomy or wedge resection) for clinical T1 (cT1) stage NSCLC may offer enhanced benefits according to the third edition of the American College of Chest Physicians (ACCP) Guidelines [4]. A large prospective study examining early-stage lung cancer (JCOG0802) [5] also demonstrated that postoperative lung function exhibited a significantly greater advantage in the segmentectomy group compared with the lobectomy group. While there was no notable difference in recurrence-free survival between the segmentectomy and lobectomy groups, the segmentectomy group exhibited a longer overall survival than the lobectomy group. Therefore, in this era of precision medicine, sublobar resection may be more suitable for patients with cT1 LUAD [6]. However, various factors can affect the prognosis of LUAD patients, including high-risk subtypes (micropapillary and solid), lymphovascular invasion (LVI), lymph node metastasis (LNM), visceral pleural infiltration (VPI), spread through air space (STAS), Ki-67 proliferative index, and genetic mutations [7–12]. Notably, patients with pathologic risk factors may be contraindicated for sublobar resection [13–17]. Preoperative identification of pathological risk factors enables more precise patient risk stratification, thereby supporting clinical decision-making and prognostic evaluation. To date, TNM staging system stands as the predominant clinical approach for evaluating the prognosis of LUAD patients [18]. Nevertheless, using this metric as the sole basis for patient stratification is limited by the substantial heterogeneity observed in LUAD. Even among patients with identical pathologic stages, variations in recurrence rates and survival rates following complete resection surgery may exist [19–22].

Radiomics has emerged as a pivotal tool to overcome this limitation. By analyzing large-scale imaging datasets, radiomics provides a noninvasive approach to quantify tumor heterogeneity through high-throughput extraction of subvisual biomarkers [23, 24]. These biomarkers systematically decode multidimensional tumor characteristics, including spatial architecture, temporal dynamics, and molecular phenotypes, thereby enabling comprehensive heterogeneity profiling [25]. Therefore, radiomics enhances diagnostic accuracy and enables robust prognostic stratification in clinical practice [26, 27]. However, most radiomics are binary classification studies based on supervisable methods. A data-driven technic known as consensus clustering, is employed to determine an appropriate number of clusters (k), a value that is typically chosen arbitrarily in unsupervised cluster analysis. Radiomics-based consensus clustering analysis is currently being used to classify tumor images in various cancers, such as breast cancer [28], glioblastoma [29] and renal clear cell carcinoma [30]. Unsupervised clustering analysis of tumor radiomic features could enable preoperative risk stratification in lung adenocarcinoma, thereby guiding personalized treatment strategies. While clinical-radiomic studies in lung adenocarcinoma have been extensively investigated [31–34], clinical-radiomic-genetic studies still lack.

Although Rocio Perez-Johnston et al. [35] have investigated the correlation of consensus clustering results based on radiomic features with the pathology and genomics of stage I LUAD, that study did not address the correlation of VPI, LNM, and Ki-67 proliferative index and other pathology risk factors. Also, the dataset they used was relatively small, and the study was more focused on genomic features. Our study aimed to utilize a larger dataset to explore the association between consensus clustering results based on radiomic features and multiple pathological risk factors of cT1 LUAD, to promote the precise treatment and prognosis prediction of early-stage LUAD in the clinic.

Materials and methods

Patient data

Patients pathologically diagnosed as LUAD and underwent surgical resection data were collected from September 2018 to May 2021 at the Department of Thoracic Surgery, Zhongshan Hospital, Fudan University. Patients' data including clinical, pathological and CT imaging data were retrospectively analyzed. Inclusion criteria: (1) patients who pathologically diagnosed as microinvasive and invasive LUAD and underwent complete surgical resection; (2) cT1 lung lesions were confirmed by the 8th edition of the American Joint Committee on Cancer (AJCC) staging system [36]. Exclusion criteria: (1) incomplete or missing clinical data, pathohistological results, and genomic data; (2) surgically or pathologically confirmed multiple primary lung cancers (≥ 2); (3) preoperative treatment such as chemotherapy, radiotherapy, and biopsy; (4) pre-existing lung cancer or history of other malignant tumors; (5) absence of thin-layer CT images

(layer thickness ≤ 2 mm) within the 2 weeks prior to the operation; (6) severe respiratory motion artifacts. A total of 497 lesions in 497 patients were included, with 164 males and 333 females, aged 23–87 (54 ± 12) years. The flowchart of case screening was shown in Fig. 1. The clinical and pathological information included age, gender, smoking history, tumor location, pathological subtype, infiltration level, LNM, VPI, LVI, STAS, Ki-67 proliferation index, and gene mutation. This retrospective study was approved by the Ethical Review Committee of Zhongshan Hospital, Fudan University.

CT image acquisition

Siemens SOMATOM Definiton AS + 128-slice spiral CT scanner and Philips Brilliance 64-slice spiral CT scanner were applied. Scanning parameters of Siemens CT machine: tube voltage 120 kV, tube current 159 mA, and pitch 0.95. Philips CT machine: tube voltage 120 kV, tube current 200 mA, and pitch 0.64. Before the scanning process, all patients underwent breath-holding training, and maintained calm breathing while holding their breath during the actual scanning procedure. The scanning area was scanned from apex pulmonis to basis pulmonis, and the two sides included the axillae and chest wall. A high-resolution reconstruction algorithm was used (Siemens CT, BF = 70; Philips CT, lung algorithm) with a reconstruction layer thickness of 1 mm and a reconstruction interval of 1 mm.

CT characterization

CT images were retrospectively analyzed by a radiologist who has 20 years' experience of chest CT imaging and has no prior knowledge of the pathological results. CT imaging signs including lesion density (solid nodule or subsolid nodule), shape (round/oval or irregular), burr sign, vacuole sign, lobular sign, pleural depression sign, and air bronchial sign were recorded. The above CT signs were defined in Table A. 1.

Detection and segmentation of lesions

The lung window image sequences of patients were imported into the uAI artificial intelligence scientific research platform (uAI Research Portal; United Imaging Intelligence, Shanghai, China) in Digital Imaging and Communications in Medicine (DICOM) format. Initially, the images underwent preprocessing, including anonymization and image normalization. Subsequently, the platform's built-in models were used for the automatic detection and segmentation of the volume of interest (VOI) for lung nodules. The deep learning model employed for this task is the V-BottleNeck Net (VB-Net), which is based on proprietary intellectual property rights. This model utilizes an integrated two-level network based on images and feature pyramid networks (FPN) and has been trained and tested on multi-center datasets. The research supporting this deep learning segmentation method has been published previously [37]. The segmentation results of pulmonary nodules were generated using the platform's built-in deep learning model and were then reviewed layer by layer by a radiologist with 20 years of experience in lung cancer imaging diagnosis, in order to make any necessary modifications (without reference to the pathological results). The delineation of the VOI depended on the tumor-lung interface, and efforts were made to exclude structures such as

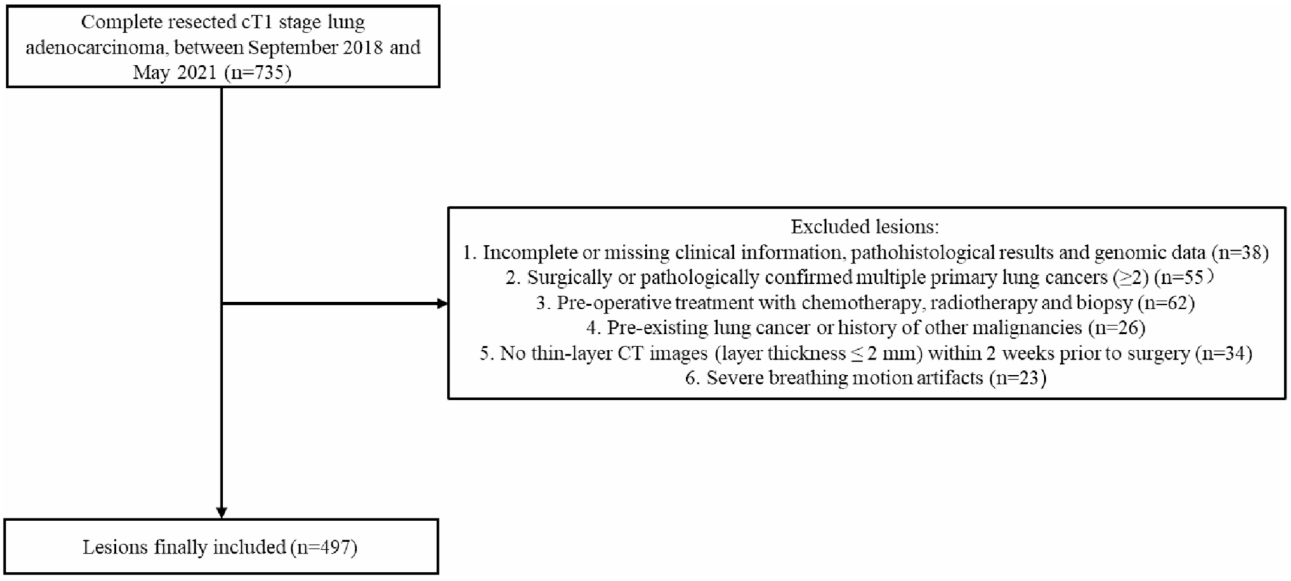

Fig. 1 The work flow of case screening process

blood vessels and bronchi as much as possible during the delineation process.

Radiomics feature extraction

The feature extraction function of the uAI artificial intelligence research platform, which is embedded with the PyRadiomics toolkit (https://pyradiomics.readthedocs.io/en/latest/index.html), was used to calculate the imaging histological features of the tumor tissue within the VOI. To mitigate the interference arising from inconsistent spatial resolution attributed to various CT models, the images were resampled to achieve a uniform pixel spacing of 1.0 mm in all three anatomical directions. High-pass or low-pass wavelet filters and Laplace of Gaussian filters were applied to assess the original CT images, which generated a total 8 wavelet-preprocessed images and 4 Laplace filter-preprocessed images. Subsequently, the histological features of both the original CT images and the preprocessed images were extracted. These features encompassed first-order features derived from the CT values or pixel values of the preprocessed images, morphological features delineating the morphology of the tumors, and texture features portraying the internal and surface texture of the tumors. Notably, the texture features comprised a gray-level difference matrix (GLDM), gray-level co-occurrence matrix (GLCM), gray-level size zone matrix (GLSZM), gray-level run length matrix (GLRLM), and neighborhood gray-tone difference matrix (NGTDM). A total of 2264 image histologic features were extracted for each lesion.

Unsupervised cluster analysis of radiomic features

Each histological quantitative feature was normalized to eliminate quantitative effects between features, and consensus clustering was performed on the extracted radiological histological features using the ConsensusClusterPlus (version 1.60.0) package for the R language. Consensus clustering is a method of integrated clustering, which aims to obtain a more stable and reliable clustering structure by combining the results of multiple clusters. The basic principle is to obtain different initial clustering results by running the clustering algorithm several times, and then merging strategies are implemented to combine these results into a final consensus clustering result. The advantage of consensus clustering is that by integrating multiple clustering results, it can reduce the dependence on the initial conditions and can weaken the noise and instability in the clustering results, thus obtaining a more robust and reliable clustering structure. Multiple iterations were conducted to determine cluster consistency of various subsamples using clustering algorithm. The optimal k-value, indicative of well-separated and stable clusters, is then selected. The implementation of this method involves iteratively subsampling 80% of the dataset for a given set of possible k values ranging from 1 to 6. Hierarchical clustering is performed on each subsample, and subsequently, the relative cluster frequency of each patient and each k value is assessed for the remaining patients. This process results in the generation of a consensus matrix. The consensus cumulative distribution function (consensus CDF), tracking plot, sample consistency (item-consensus, IC) and cluster-consensus (CLC) were used to determine the optimal k-value and evaluate the effect of consensus clustering.

Pathological assessment

All patients underwent open or televised thoracoscopic surgery involving radical resection coupled with lymph node dissection, where radical resection comprised both lobectomy and sublobar resection (segmental or wedge resection). Following the resection, the specimens underwent routine fixation, embedding, sectioning, staining, and examination under a microscope at 200x magnification to establish a pathological diagnosis in accordance with the World Health Organization NSCLC classification [38]. All resected lymph nodes were analyzed microscopically for metastatic infiltration using hematoxylin-eosin (HE) staining. The hilar and mediastinal lymph nodes were delineated with reference to IASLC LN charts [39]. VPI was considered positive when tumor cells were beyond the pleural elastic lamina as determined by elastic staining [40]. According to the 2015 WHO Classification of lung cancer, STAS was characterized by clusters of pathological micropapillae, solid nests, or single cells extending beyond the main tumor margins [11]. According to a previous study [41], a Ki-67 PI expression level of 10% was designated as the cutoff for distinguishing high and low expression. Consequently, specimens were categorized into two groups: Ki-67 PI high expression group (Ki-67 ≥ 10%) and Ki-67 PI low expression group (Ki-67 < 10%). Two pathologists histopathologically analyzed the surgically resected specimens at a consensus conference to establish a final diagnosis.

Tumor gene testing

The analytical procedures were conducted following the methodology outlined in previous studies [42]. In summary, we formulated reverse transcriptase polymerase chain reaction primers designed to encompass the mutational hotspot regions of common driver genes involving *EGFR*, *HER2*, *KRAS*, and *BRAF*. In addition, the translocations of *ALK*, *ROS1*, and *RET* were identified through a real-time reverse transcriptase polymerase chain reaction-based quantitative fusion assay, which was subsequently validated using fluorescence in situ hybridization.

Statistical analysis

R software version 3.6.1 (R Foundationfor Statistical Computing) and SPSS were used for all analyses. Consensus clustering of the extracted radiomic features was performed using the ConsensusClusterPlus (version 1.60.0) package for the R language. SPSS software was implemented to figure out whether the resulting clusters were associated with clinical features, CT features, pathological features, and gene expression features. Comparisons between groups of count data were performed using chi-square test or Fisher's exact test. The normality was measured using the Shapiro-Wilk test. Count data, following a normal distribution expressed as x ± s, and those not conforming to a normal distribution expressed as M (Q1, Q3). Mann-Whitney U test was employed to analyze the difference between two groups. All hypothesis tests were two-sided, with a significance level set at $P < 0.05$ to denote statistical significance.

Table 1 Clinical and CT characteristics by cluster

Variable	All ($n=497$)	Cluster 1 ($n=258$)	Cluster 2 ($n=239$)	*p* Value
Age(y) [#]	56 (48, 63)	59 (50, 65)	54 (43, 60)	< 0.001[&]
Gender				0.722[#]
Male	164 (33.0)	87 (33.7)	77 (32.2)	
Female	333 (67.0)	171 (66.3)	162 (67.8)	
Smoking history				0.461
No	457 (92.0)	235 (91.1)	222 (92.9)	
Yes	40 (8.0)	23 (8.9)	17 (7.1)	
Surgical modalities				0.022
Sublobar resection	215 (43.3)	99 (38.4)	116 (48.5)	
Lobectomy	282 (56.7)	159 (61.6)	123 (51.5)	
Location				0.928
Left upper lobe	128 (25.8)	67 (26.0)	67 (25.5)	
Left lower lobe	76 (15.3)	39 (15.1)	37 (15.5)	
Right upper lobe	160 (32.2)	38 (31.4)	79 (33.1)	
Right middle lobe	41 (8.2)	9 (9.3)	17 (7.1)	
Right lower lobe	92 (18.5)	23 (18.2)	45 (18.8)	
Density				< 0.001[*]
SSN	439 (88.3)	201 (77.9)	238 (99.6)	
SN	58 (11.7)	57 (22.1)	1 (0.4)	
Shape				< 0.001
Round/Oval	173 (34.8)	47 (18.2)	126 (52.7)	
Irregular	324 (65.2)	211 (81.8)	113 (47.3)	
Spiculation				< 0.001
No	381 (76.7)	157 (60.9)	224 (93.7)	
Yes	116 (23.3)	101 (39.1)	15 (6.3)	
Lobulation				< 0.001
No	395 (79.5)	170 (65.9)	225 (94.1)	
Yes	102 (20.5)	88 (34.1)	14 (5.9)	
Vacuole				0.841
No	452 (90.9)	234 (90.7)	218 (91.2)	
Yes	45 (9.1)	24 (9.3)	21 (8.8)	
Pleural indentation				< 0.001
No	319 (64.2)	136 (52.7)	183 (76.6)	
Yes	178 (35.8)	122 (47.3)	56 (23.4)	
Air bronchogram				< 0.001
No	314 (63.2)	128 (49.6)	186 (77.8)	
Yes	183 (36.8)	130 (50.4)	503(22.2)	
CT size (mm) [#]	12 (9, 16)	14 (11, 18)	10 (8, 13)	< 0.001[&]

Note: Unless otherwise indicated, data are numbers of patients and data in parentheses are percentages. [#] Data in parentheses are the interquartile range. [&] Mann-Whitney U test; [*] Fisher's exact probability test. The rest are chi-square tests

Results

Clinical and CT morphologic data of patients

The clinical and CT morphologic data of 497 enrolled patients were shown in Table 1. The median age of the patients were 56 years (interquartile range [IQR], 48–63 years). 164 patients (33.0%) were male, and 333 (67.0%) were female, with most of them were nonsmokers ($n=457$, 92.0%). All patients underwent R0 resection, with the most common procedure was lobectomy ($n=282$, 56.7%), followed by sublobar resection ($n=215$, 43.3%). The upper lobe of the left lung was identified as the most prevalent site of lesion occurrence ($n=128$, 25.8%). In terms of CT morphology, the two clusters were statistically different in density classification, shape, burr, lobulation, pleural pull, air bronchial sign and CT size ($p<0.001$). No statistically significant difference in the vacuolar sign was observed between the two clusters ($p=0.841$).

Consensus clustering results based on CT radiomics

The final results confirmed the optimal k value = 2. Therefore, 497 cases were divided into 2 clusters, with 258 (51.9%) cases in Cluster 1 and 239 (48.1%) cases in Cluster 2. Figure 2 displayed the assessment of data clustering when k value was set from 2 to 6, where the heatmap generated based on the consistency matrix legend was shown in Fig. 2A, and Fig. 2B-F showed the heatmap of the consistency matrix for different k values (number of categories). Figure 3A presented the CDF distribution for different k values. Larger values of CDF distribution area indicated more robust clustering results for that k value. Figure 3B showed the delta area plot, a linear plot employed to aid in determining the optimal number of clusters. This plot illustrated the relative change in the area under the CDF curve for k and k-1 in comparison to k. Larger values indicated a more pronounced improvement in the superiority of the clustering results for that value of k compared to the clustering results for k-1. In this study, the CDF distribution was smoother when k = 2 and the area under the CDF curve was largest when k = 2, after which the enhancement was not obvious, so the clustering results were the optimal when k = 2. The sample consistency (item-consensus, IC) was delineated in Fig. 3C, which was the average consistency value between a sample and a member of a clustering cluster. Therefore,

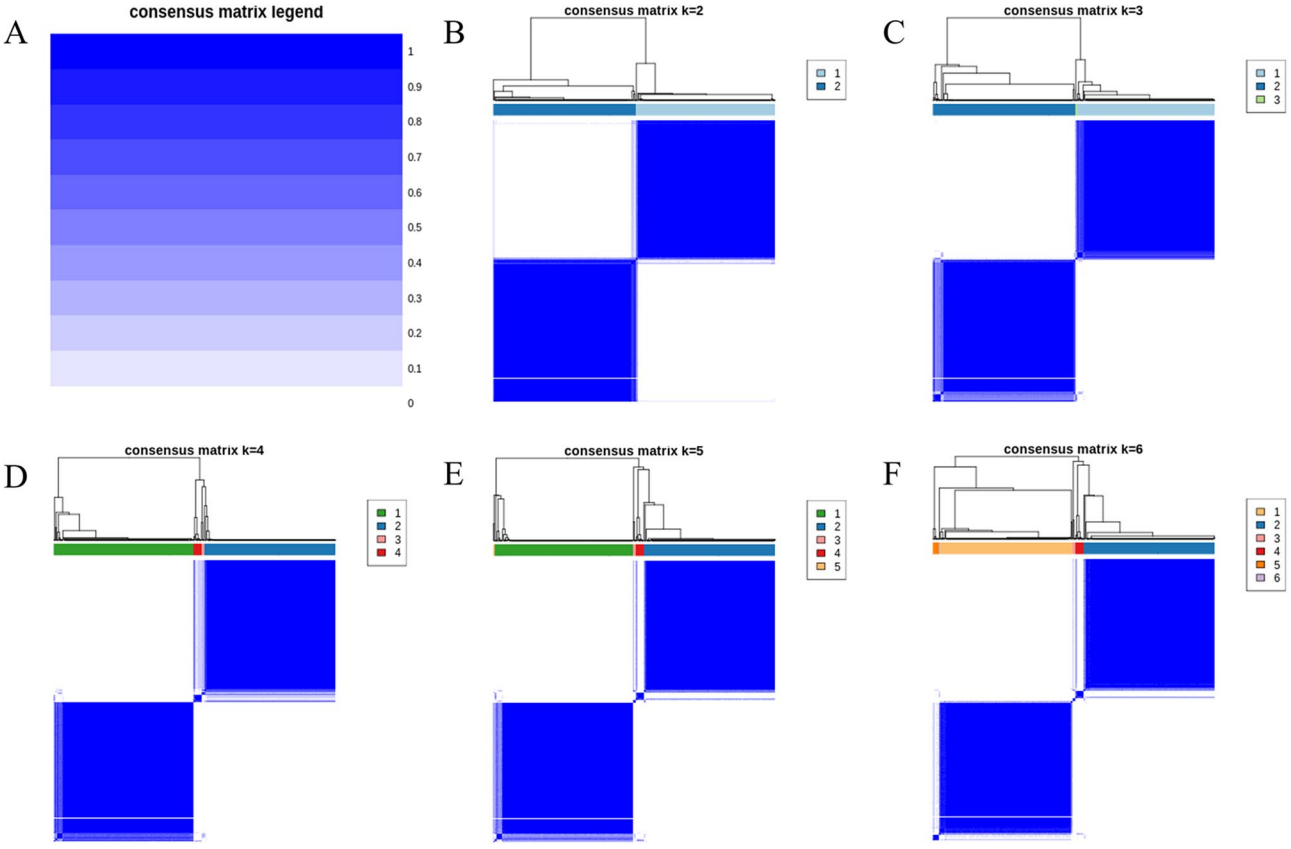

Fig. 2 Results of data subtyping for each case of the number of clusters k = 2 to 6. (**A**) The heatmap generated based on the consistency matrix. (**B-F**) Heatmaps of the consistency matrix for different k values (number of categories)

a sample had multiple IC values corresponding to k clusters at different number k. Based on the IC values of this sample in different clustering clusters, it was determined into which cluster this sample should be classified. For a given sample, if it has a greater proportion of IC values in a certain clustering cluster, it indicates that its classification is stable, while if its IC values in different clustering clusters do not differ much, it indicates that their classification may be unstable. Figure 3D showed tracking plot which was used to visualize the variation of clustering results with different clusters. It described the similarities and differences between the clustering results for different clusters. The columns represent the samples, the rows represent each k-value, and the colors indicate the categories in the consistency matrix. With the tracking plot, it is possible to observe whether the clustering results are relatively stable and whether there is any significant divergence and shift. If the categories of a sample change frequently, it means that the sample is an unstable sample, and the class containing a large number of such samples is also an unstable class. It can be seen from the figure that when k = 2, the samples can be stably classified. Figure 3E showed cluster-consensus (CLC), which represents the average IC between pairs of samples in a consistent cluster. The higher value represents the higher stability, which can help to assess whether the superiority of the clustering effect of increasing k value is elevated compared to the current k value. Figure 3A-E all confirmed that the clustering effect was the optimal when k = 2.

Consensus clustering associations

Correlation of consensus clustering results with pathology: the comparison results of pathologic risk factors in different clusters were shown in Table 2. In general, Cluster 1 is associated with more aggressive tumor features (higher Ki-67, more micropapillary/solid components, higher STAS, VPI, and LNM rates). Specifically, Cluster 1 contained a higher proportion of IAC compared to Cluster 2 (94.6% vs. 62.3%, $p < 0.001$). Cluster 1 consisted of more cases with micropapillary component and solid component than Cluster 2 (27.1% vs. 1.3%, $p < 0.001$; 10.5% vs. 1.4%, $p < 0.001$). Cluster 1 was more likely to develop lymph node metastases (2.3% vs. 0%, $p = 0.031$), VPI (5.4% VS 1.3%, $p = 0.012$), and STAS (8.1% vs. 0%, $p < 0.001$) than Cluster 2. Cluster 1 had more cases of high Ki-67 expression than Cluster 2 (38.4% vs. 14.6%, $p < 0.001$). Although Cluster 1 was not statistically

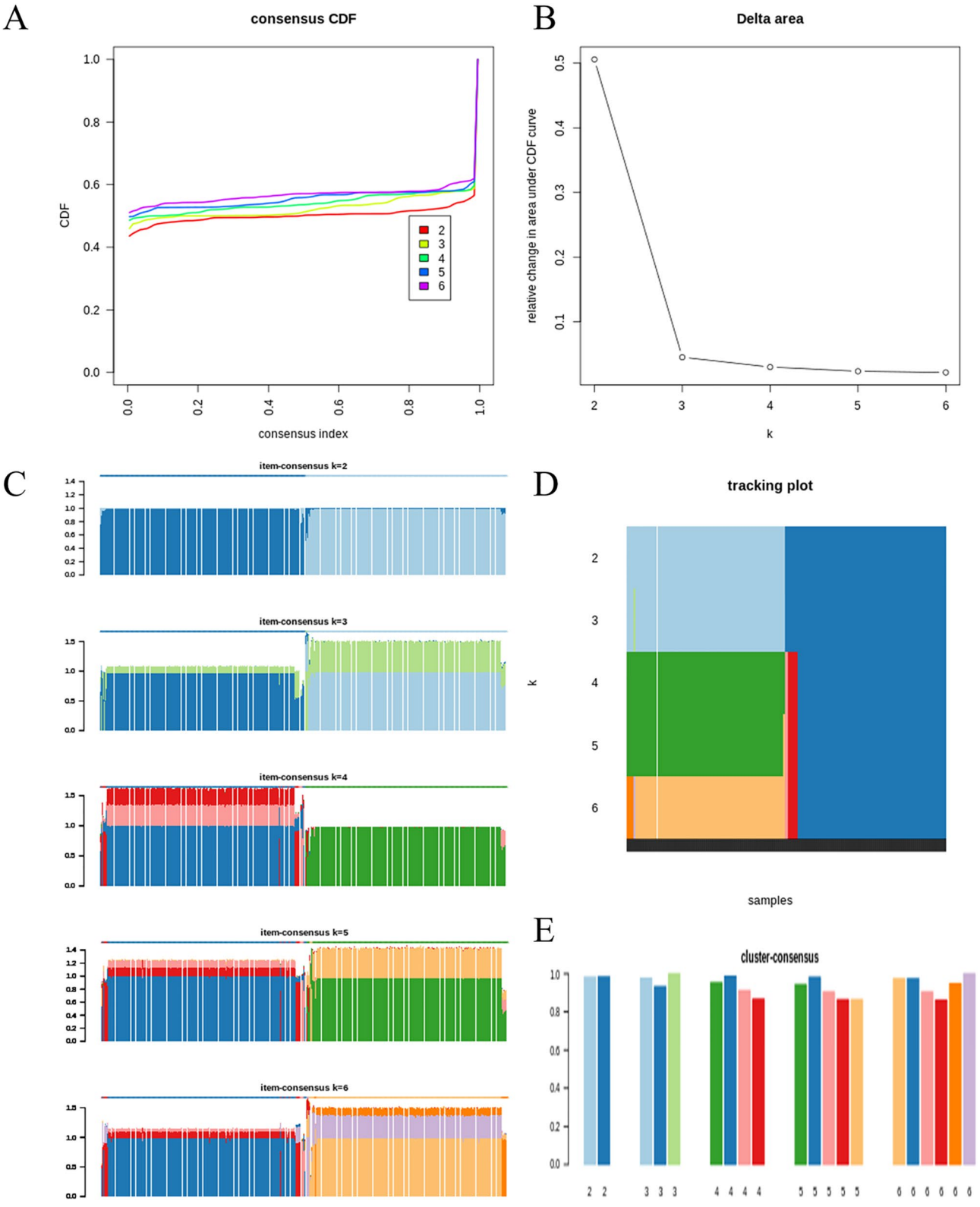

Fig. 3 Consensus clustering for radiomic stratification of patients. (**A**) The probability cumulative distribution function (CDF) distribution for each k. (**B**) The delta plot highlights the relative change between k and k – 1 under the CDF curve. (**C**) Sample Consensus (IC) plot, showing the average consistency value between a sample and a member of a clustered cluster. (**D**) Tracking plot with columns for samples, rows for each k-value, and colors indicating categories in the consistency matrix. (**E**) Cluster-consensus (CLC) plot, which represents the average IC between pairs of samples in a consistency clustering cluster

Table 2 Pathological risk factors by cluster

Variable	All (*n* = 497)	Cluster 1 (*n* = 258)	Cluster 2 (*n* = 239)	*p* Value
Pathology type				< 0.001
MIA	104 (20.9)	14 (5.4)	90 (37.7)	
IAC	393 (79.1)	244 (94.6)	149 (62.3)	
Micropapillary				< 0.001*
No	424 (85.3)	188 (72.9)	236 (98.7)	
Yes	73 (14.7)	70 (27.1)	3 (1.3)	
Solid				< 0.001*
No	469 (94.4)	231 (89.5)	238 (99.6)	
Yes	28 (5.6)	27 (10.5)	1 (1.4)	
LNM				0.031*
No	491 (98.8)	252 (97.7)	239 (100)	
Yes	6 (1.2)	6 (2.3)	0 (0)	
VPI				0.012*
No	480 (96.6)	244 (94.6)	236 (98.7)	
Yes	17 (3.4)	14 (5.4)	3 (1.3)	
LVI				0.125*
No	493 (99.2)	254 (98.4)	239 (100)	
Yes	4 (0.8)	4 (1.6)	0 (0)	
STAS				< 0.001*
No	476 (95.8)	237 (91.9)	239 (100)	
Yes	21 (4.2)	21 (8.1)	0 (0)	
Ki-67				< 0.001
Low	363 (73.0)	159 (61.6)	204 (85.4)	
High	134 (27.0)	99 (38.4)	35 (14.6)	

Note: Data are numbers of patients and data in parentheses are percentages. * Fisher's exact probability test. The rest are chi-square tests. MIA = microinvasive adenocarcinoma, IAC = invasive lung adenocarcinoma, LNM = lymphatic node metastasis, VPI = visceral pleural invasion, LVI = lymphovascular invasion, STAS = spread through air spaces

Table 3 Mutation frequencies by cluster

Variable	All (*n* = 497)	Cluster 1 (*n* = 258)	Cluster 2 (*n* = 239)	*p* Value
EGFR				0.125
Wild	205 (41.2)	98 (38.0)	107 (44.8)	
Mutation	292 (58.8)	160 (62.0)	132 (55.2)	
HER2				< 0.001
Wild	462 (93.0)	252 (97.7)	210 (87.9)	
Mutation	35 (7.0)	6 (2.3)	29 (12.1)	
KRAS				0.196
Wild	467 (94.0)	239 (92.6)	228 (95.4)	
Mutation	30 (6.0)	19 (7.4)	11 (4.6)	
ROS1				0.374*
Wild	492 (99.0)	254 (98.4)	238 (99.6)	
Mutation	5 (1.0)	4 (1.6)	1 (0.4)	
RET				0.265*
Wild	484 (97.4)	248 (96.5)	235 (98.3)	
Mutation	13 (2.6)	9 (3.5)	4 (1.7)	
BRAF				1.000*
Wild	495 (99.6)	257 (99.6)	238 (99.6)	
Mutation	2 (0.4)	1 (0.4)	1 (0.4)	
ALK				0.065*
Wild	486 (97.8)	249 (96.5)	237 (99.2)	
Mutation	11 (2.2)	9 (3.5)	2 (0.8)	

Note: Data are numbers of patients and data in parentheses are percentages. * Fisher's exact probability test. The rest are chi-square tests

different from Cluster 2 in LVI expression (1.6% vs. 0%, $p = 0.125$), all 4 LVI cases were included in Cluster 1.

Correlation between consensus clustering results and gene expression: the comparison results of gene mutation frequencies in different clusters were shown in Table 3. It was worth emphasizing that only HER2 mutation frequency displayed significant difference between Cluster 1 and 2 ($p < 0.001$), and no statistically significant difference was shown in the other mutations ($p > 0.05$). Among 497 enrolled cases, the most common type of gene mutation was *EGFR* mutation ($n = 292$, 58.8%), of which 162 cases had mutations in exon 21, 109 cases in exon 19, 14 cases in exon 20, 4 cases in exon 18, 1 case in both exon 18 and 20, 1 case in both exon 19 and 20, and 1 case in both exon 20 and 21. The mutation frequencies of other mutations were *HER2* (7%), *KRAS* (6%), *ROS1* (1%), *RET* (13%), *BRAF* (2%), and *ALK* (11%).

The comparison results of the pathological risk factors in different clusters of invasive LUAD subgroup were shown in Table 4. Similar to the overall results, Cluster 1 had a higher incidence of pathologic risk factors relative to Cluster 2. In invasive LUAD, the two clusters were statistically different in terms of pathological grading, micropapillary component, solid component, STAS, and Ki-67 expression (all $p < 0.001$). Although Cluster 1 showed more lymph node metastasis, VPI and LVI than Cluster 2 (2.5% vs. 0%, 5.7% vs. 2.0%, 1.6% vs. 0%), there was no statistical difference ($p = 0.087$, $p = 0.078$, $p = 0.302$).

The comparison results of pathologic risk factors in different clusters of the subsolid subgroups were shown in Table 5. In subsolid nodules, two clusters were statistically different in terms of pathologic type ($p < 0.001$), micropapillary component ($p < 0.001$), solid component ($p < 0.001$), STAS ($p = 0.009$), and Ki-67 expression ($p < 0.001$). There was no statistical difference in LNM, VPI and LVI ($p > 0.05$). The comparison results of the frequency of gene mutations between two clusters in invasive LUAD were shown in Table A. 2. Cluster 1 and Cluster 2 were statistically different only in HER2 mutation ($p < 0.001$), and no statistical difference was observed in all other gene mutations ($p > 0.05$). The comparison results of the frequency of gene mutations in subsolid nodules between two clusters were shown in Table A. 3. It was noteworthy that Cluster 1 and Cluster 2 were statistically different in *EGFR* ($p = 0.031$) and *HER2* mutations ($p < 0.001$), and no statistically significant difference was shown in all other gene mutations ($p > 0.05$).

Pathological and genomic variables OncoPrint for two clusters were shown in Fig. 4. Examples of cases per cluster were displayed in Fig. 5.

Table 4 Pathological risk factors by cluster in IAC

Variable	All (*n* = 393)	Cluster 1 (*n* = 244)	Cluster 2 (*n* = 149)	*p* Value
Pathological grade				< 0.001
I	48 (12.2)	20 (8.2)	28 (18.8)	
II	307 (78.1)	187 (76.6)	120 (80.5)	
III	38 (9.7)	37 (15.2)	1 (0.7)	
Micropapillary				< 0.001*
No	320 (92.9)	174 (71.3)	146 (98.0)	
Yes	73 (7.1)	70 (28.7)	3 (2.0)	
Solid				< 0.001*
No	365 (92.9)	217 (88.9)	148 (99.3)	
Yes	28 (7.1)	27 (11.1)	1 (0.7)	
LNM				0.087*
No	387 (98.5)	238 (97.5)	149 (100)	
Yes	6 (1.5)	6 (2.5)	0(0)	
VPI				0.078*
No	376 (95.7)	230 (94.3)	146 (98.0)	
Yes	17 (4.3)	14 (5.7)	3 (2.0)	
LVI				0.302*
No	389 (99.0)	240 (98.4)	149 (100)	
Yes	4 (1.0)	4 (1.6)	0 (0)	
STAS				< 0.001*
No	372 (94.7)	223 (71.3)	149 (100)	
Yes	21 (5.3)	21 (28.7)	0 (0)	
Ki-67				< 0.001
Low	263 (66.9)	145 (59.4)	118 (79.2)	
High	130 (33.1)	99 (40.6)	31 (20.8)	

Note: Data are numbers of patients and data in parentheses are percentages. * Fisher's exact probability test. The rest are chi-square tests. LNM = lymphatic node metastasis, VPI = visceral pleural invasion, LVI = lymphovascular invasion, STAS = spread through air spaces

Table 5 Pathological risk factors by cluster in SSN

Variable	All (*n* = 439)	Cluster 1 (*n* = 201)	Cluster 2 (*n* = 238)	*p* Value
Pathology type				< 0.001
MIA	104 (23.7)	14 (7.0)	90 (37.8)	
IAC	335 (76.3)	187 (93.0)	148 (62.2)	
Micropapillary				< 0.001*
No	401 (91.3)	165 (82.1)	236 (99.2)	
Yes	38 (8.7)	36 (17.9)	2 (0.8)	
Solid				< 0.001*
No	430 (97.9)	193 (96.0)	237 (99.6)	
Yes	9 (2.1)	8 (4.0)	1 (0.4)	
LNM				0.209*
No	437 (99.5)	199 (99.0)	238 (100)	
Yes	2 (0.5)	2 (1.0)	0 (0)	
VPI				0.197*
No	429 (97.7)	194 (96.5)	235 (98.7)	
Yes	10 (2.3)	7 (3.5)	3 (1.3)	
LVI				0.458*
No	438 (99.8)	200 (99.5)	238 (100)	
Yes	1 (0.2)	1 (0.5)	0 (0)	
STAS				0.009*
No	433 (98.6)	195 (97.0)	238 (100)	
Yes	6 (1.4)	6 (3.0)	0 (0)	
Ki-67				< 0.001
Low	346 (78.8)	142 (70.6)	204 (85.7)	
High	93 (21.2)	59 (29.4)	34 (14.3)	

Note: Data are numbers of patients and data in parentheses are percentages. * Fisher's exact probability test. The rest are chi-square tests. MIA = microinvasive adenocarcinoma, IAC = invasive lung adenocarcinoma, LNM = lymphatic node metastasis, VPI = visceral pleural invasion, LVI = lymphovascular invasion, STAS = spread through air spaces

Discussion

In this study, we divided 497 patients with cT1 LUAD into two clusters using a consensus clustering method based on CT radiomics, and found that Cluster 1 correlated with high-risk pathologic factors for cT1 LUAD. Particularly, statistically significant differences were shown in micropapillary component, solid component, STAS, and Ki-67 expression between two clusters, as well as in the subgroup analysis of invasive adenocarcinomas and subsolid lesions. Our study suggests that radiomic features are heterogeneous and that consensus clustering methods based on CT radiomics have the potential for risk stratification, precise treatment and prognostic prediction for cT1 LUAD.

Previous research suggested that invasive adenocarcinoma subtype is an important factor affecting prognosis independent of TNM staging [11]. It has been proposed that the presence or absence of LVI is a crucial factor influencing the prognosis of patients with stage IA [43, 44]. Both LVI and VPI are considered as invasive growth patterns and are often discussed together. In the study by Wang et al. [45], both LVI and VPI were regarded as independent risk factors for RFS in stage I NSCLC patients with tumor size ≤ 3 cm, and they found that LVI and VPI together for prognostic stratification better differentiated patients' prognosis. In early-stage LUAD, STAS is also a prognostic risk factor, with a 5-year disease-free survival of 70-80% in patients with STAS undergoing radical surgical resection [7, 46]. Previous studies have recognized the Ki-67 proliferation index as a prognostic biomarker for LUAD [9, 21]. However, the results of these pathologic risk factors are only available after postoperative pathologic analysis, making preoperative diagnosis difficult. Nevertheless, the advent of radiomics has made it possible for the non-invasive assessment of microscopic features of tumor pathology.

A group of evidences have shown that imaging histology has a better performance in identifying high risk factors for a particular pathology [47–51]. However, these studies are based on binary classification results from supervisable methods. In this study, an unsupervised consensus clustering approach was innovatively adopted to mine the relationship between CT images and pathological micro-features and gene expression. The integrated analysis of medical images and multi-omics molecular data serves to bridge the gap between

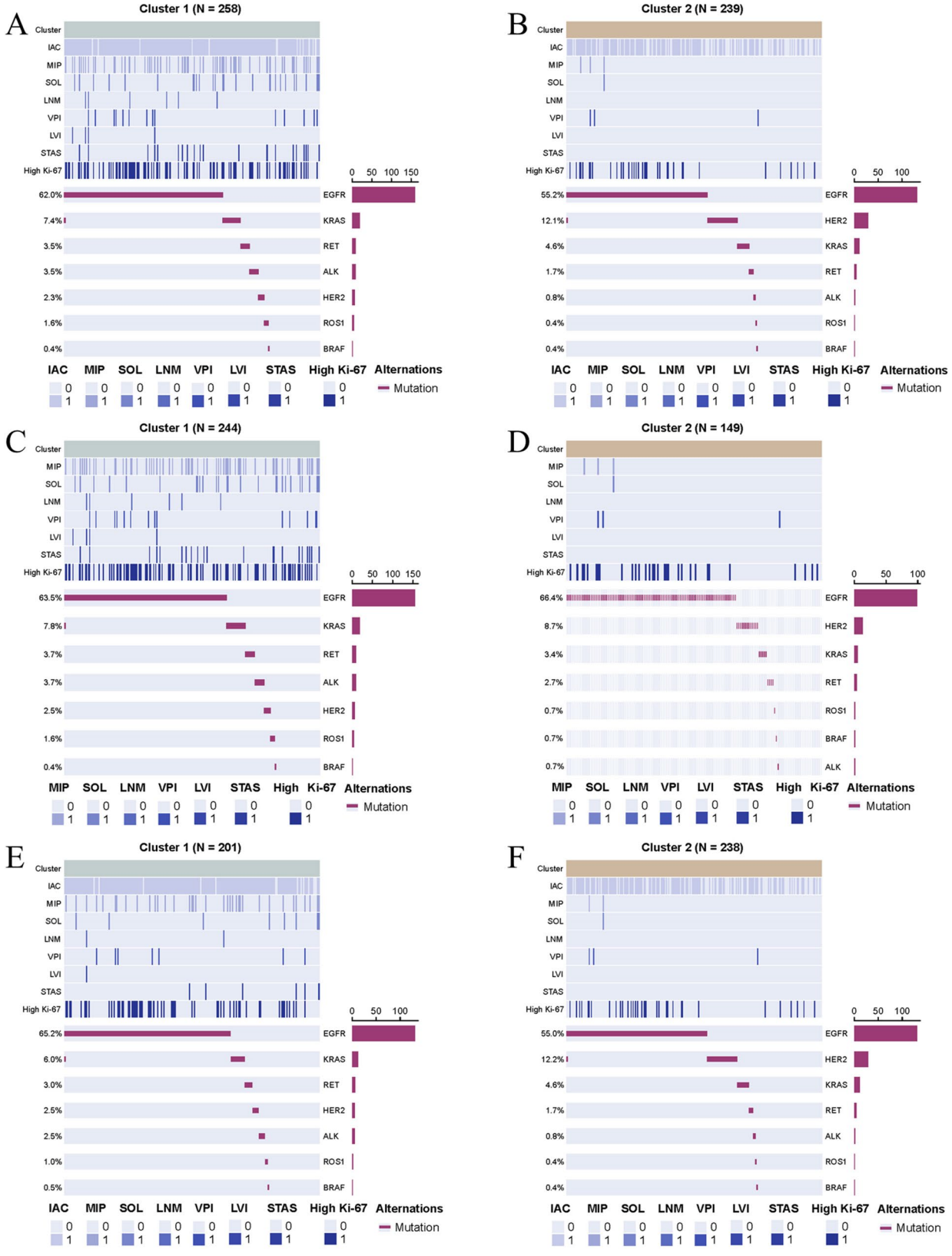

Fig. 4 (See legend on next page.)

(See figure on previous page.)

Fig. 4 OncoPrint of pathologic and genomic variables for all cT1 LUAD patients, decomposed by radiomics consensus clustering. Columns represent patients in each radiomics feature cluster and rows represent all individually analyzed pathologic risk factors and mutation frequencies. (**A-B**) OncoPrint of pathologic and genomic variables for all patients in Cluster 1 (**A**) and Cluster 2 (**B**). (**C-D**) OncoPrint of pathologic and genomic variables for patients in the subgroup of patients with invasive LUAD in Cluster 1 (**C**) and Cluster 2 (**D**). (**E**) OncoPrint of pathology and genomic variables for patients in the Cluster 1 subsolid nodule subgroup. (**F**) OncoPrint of pathology and genomic variables for patients in the Cluster 2 subsolid nodule subgroup. IAC, invasive lung adenocarcinoma; LNM, lymphatic node metastasis; LVI, lymphovascular invasion; MIA, microinvasive adenocarcinoma; MIP, micropapillary; SOL, solid; STAS, spread through air spaces; VPI, visceral pleural invasion

our comprehension of macroscopic medical images and microscopic molecular correlations, which helps in patient risk stratification [52].

Our results showed that patients in Cluster 1 had a relatively older age and larger tumor size ($p < 0.001$). Additionally, Cluster 1 was significantly associated with imaging signs such as solid nodules (SN), irregular shape, spiculation, lobulation, pleural depression, and air bronchus (all $p < 0.001$). Genomic analysis illustrated that Cluster 1 and Cluster 2 were statistically different only in the *HER2* gene mutation ($p < 0.001$), and none of the other gene mutations were statistically different ($p > 0.05$). In contrast, Rocio Perez-Johnston et al. [35] showed that *EGFR* was statistically different between the clusters of their clustering results, but their study did not address the *HER2* gene. *EGFR* mutations are a predominant driver gene variant subtype in LUAD. Some studies have demonstrated that *EGFR*-mutated types have an elevated risk of brain and bone metastases compared to non-*EGFR*-mutated patients [53]. In the contrary, some researchers have suggested that patients with *EGFR* mutations have a better prognosis [54, 55]. A recent study reported that *EGFR* mutations are only found in LUAD presenting as solid nodules, which may imply a higher probability of recurrence after surgery [56]. The results of this study reflect that *EGFR* mutations are not significantly correlated with LUAD aggressiveness. Human epidermal growth factorreceptor-2 (*HER2*), a member of the tyrosine kinase receptor family, has been identified in recent years as one of the rare driver genes in NSCLC. In clinical practice, the prognostic role and mechanism of *HER2* in breast cancer and gastric cancer have been well defined and widely used to guide clinical treatment. However, in NSCLC, the relationship between *HER2* mutation and prognosis is still controversial. Some studies have revealed that *HER2* mutations portend a poor prognosis [57]. However, Toh et al. [58] reported that *HER2* mutations were not associated with prognosis in 109 East Asian female LUAD patients. Meanwhile, some other researcher proposed that *HER2* mutations were negatively correlated with the prognosis of NSCLC [59]. The present study revealed that *HER-2* mutations were associated with low invasiveness of Cluster 2, which indicated that early-stage LUAD patients with *HER2* mutations may portend a favorable prognosis.

The results of this study presented that Cluster 1 was associated with IAC ($p < 0.001$), micropapillary ($p < 0.001$) and solid components ($p < 0.001$), as well as lymph node metastasis ($p = 0.031$), VPI ($p = 0.012$), STAS ($p < 0.001$), and high Ki-67 expression ($p < 0.001$). Despite the absence of a statistically significant difference in lymphovascular invasion (LVI) prevalence between Cluster 1 and Cluster 2 ($p = 0.125$), all four LVI-positive cases were exclusively identified in Cluster 1. This lack of statistical significance is likely attributable to the limited sample size of LVI-positive cases in our early-stage LUAD cohort. In the subgroup analysis of invasive LUAD, two clusters were statistically different in terms of pathologic grade ($p < 0.001$), micropapillary component ($p < 0.001$), solid component ($p < 0.001$), STAS ($p < 0.001$), and Ki-67 expression ($p < 0.001$). Although more LNM, VPI, and LVI were observed in Cluster 1 compared to Cluster 2 in invasive LUAD (2.5% vs. 0%, 5.7% vs. 2.0%, and 1.6% vs. 0%), there was no statistically significant difference between two clusters ($p = 0.087$, $p = 0.078$, and $p = 0.302$, respectively), which may also be attributable to the small number of positive case. As almost all solid nodules were in Cluster 1 (57/58), subgroups of solid density nodules were not analyzed in this study. Instead, in the sub-solid density subgroup analysis, two clusters were statistically different in terms of pathologic type ($p < 0.001$), micropapillary component ($p < 0.001$), solid component ($p < 0.001$), STAS ($p = 0.001$), and Ki-67 expression ($p < 0.001$). While there was no statistical difference in lymph node metastasis, VPI, and LVI ($p > 0.05$). Rocio Perez-Johnston et al. [35] showed statistically significant differences in micropapillary/solid component predominance, STAS and LVI among four clusters, but not in subsolid subgroup analysis.

This study has several limitations. First, there might be an unavoidable selection bias because of a retrospective study. Second, the samples contained a large majority of subsolid nodules and relatively few solid nodules, and this imbalance may have had some impact on the clustering results. Limitations such as sample imbalance and retrospective design need to be further validated in prospective studies. Third, because our sample data were early stage LUAD images where patient survival may be high, so the effect of the consensus clustering results in actually predicting patient prognosis remains to be further investigated.

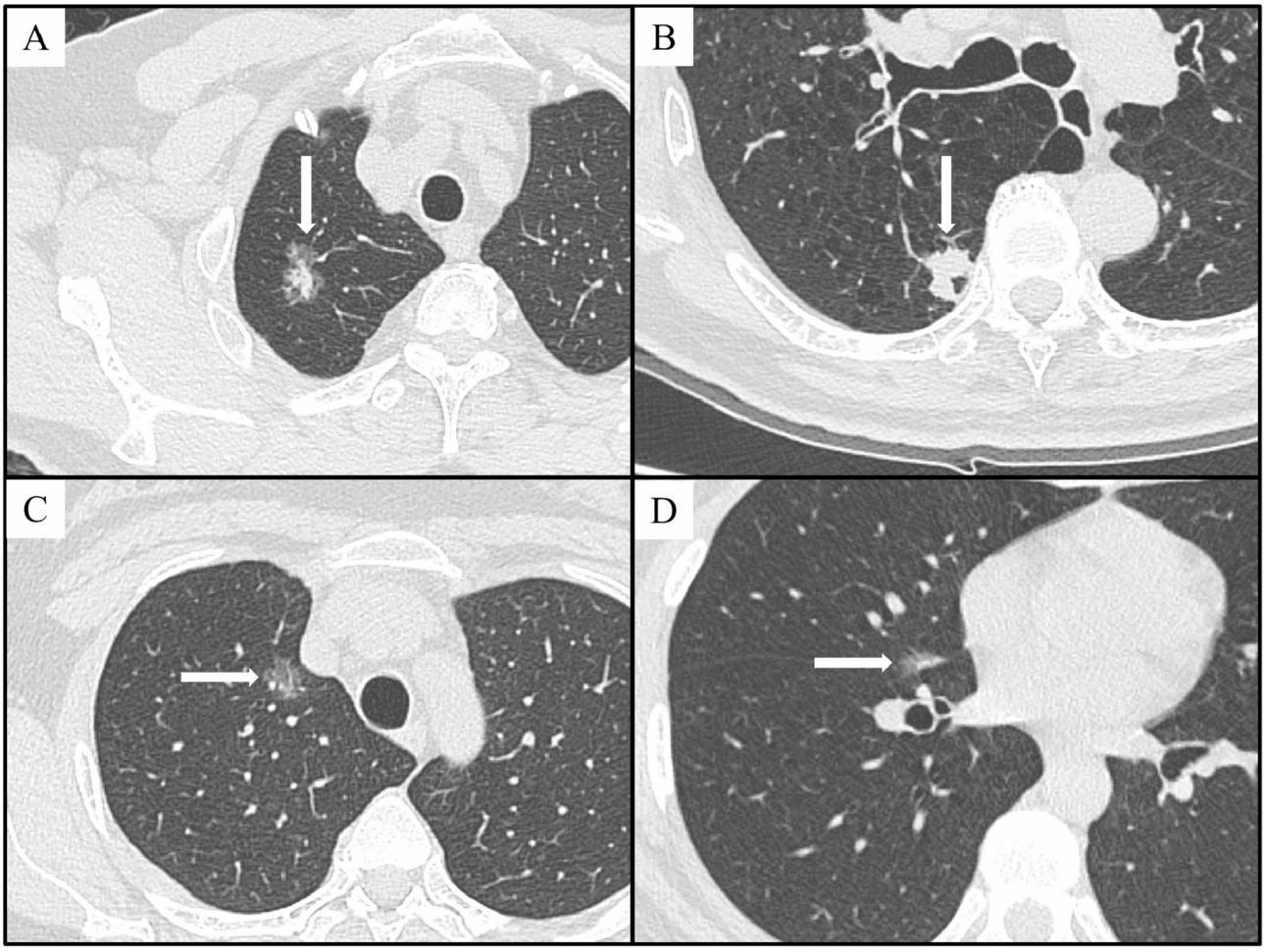

Fig. 5 Thin-section CT images of the lesion used for radiological clustering analysis. (**A**) Cluster 1. A subsolid nodule (arrow) in the upper lobe of the right lung, approximately 22 mm in length and diameter, predominantly micropapillary subtype and partially alveolar subtype, histologic grade III, STAS in the surrounding lung tissues, metastasis to the parabronchial lymph nodes, Ki-67 expression fraction of 70%, and *EGFR* mutation of exon 21. (**B**) Cluster (1) A solid nodule (arrow) in the lower lobe of the right lung, approximately 18 mm in length and diameter, solid and micropapillary histologic subtypes, histologic grade III, STAS positive, cancerous tissues involving the pleura of the visceral layer, and a Ki-67 expression fraction of 60%. (**C**) Cluster (2) A subsolid nodule (arrow) in the upper lobe of the right lung, approximately 13 mm in length, with a predominant pathological subtype of alveolar, histologic grade II; Ki-67 expression fraction of 5%, and a mutation in exon 21 of *EGFR*. (**D**) Cluster 2. A subsolid nodule (arrow) in the middle lobe of the right lung, approximately 12 mm in diameter, with a predominantly alveolar and adnexal phenotype, histologic grade II, Ki-67 expression fraction of 5%, and *RET* gene fusion

Conclusions

In summary, our study effectively highlights the role of CT radiomics in risk stratification for cT1 LUAD patients. The use of consensus clustering in exploring CT features and molecular data provides an innovative approach to prognosis prediction. The findings on *HER2* mutations and their association with low invasiveness in Cluster 2 add value to understanding LUAD prognosis. The statistical differences in pathological features between clusters suggested potential for personalized treatment strategies in LUAD.

Abbreviations

LUAD	Lung Adenocarcinoma
NSCLC	Non-small Cell Lung Cancer
ACCP	American College of Chest Physicians
LVI	LymphoVascular Invasion
LNM	Lymph Node Metastasis
VPI	Visceral Pleural Infiltration
STAS	Spread Through Air Space
AJCC	American Joint Committee on Cancer
DICOM	Digital Imaging and Communications in Medicine
VOI	Volume Of Interest
VB-Net	V-BottleNeck Net
FPN	Feature Pyramid Networks
GLDM	Gray-Level Difference Matrix
GLCM	Gray-Level Co-occurrence Matrix
GLSZM	Gray-Level Size Zone Matrix
GLRLM	Gray-Level Run Length Matrix
NGTDM	Neighborhood Gray-Tone Difference Matrix
CDF	Cumulative Distribution Function
IC	Item-Consensus
CLC	Cluster-Consensus
IQR	Interquartile Range

Supplementary Information

The online version contains supplementary material available at https://doi.org/10.1186/s12880-025-01795-x.

Supplementary Material 1

Acknowledgements
We thank Home for Researchers editorial team (www.home-for-researchers.com) for language editing service. This work was supported by the National Science Foundation of China (grant numbers 82071990, 81571629); Zhejiang Provincial Health Science and Technology Project (grant numbers 2023RC252, 2024KY252); Hangzhou Agricultural and Social Development Scientific Research Guidance Project (grant number 20220919Y078); and Policy Guidance Project of Major Science and Technology Plan for Social Development of Xiaoshan District (grant numbers 2021309, 2022327, 2022334).

Author contributions
HD, YL and LZ wrote the manuscript and analyzed the data. LY and XG conducted the data collection and analysis. XY and XX had primary responsibility for the final content.

Funding
This research was funded by the National Science Foundation of China (grant numbers 82071990, 81571629); Zhejiang Provincial Health Science and Technology Project (grant numbers 2023RC252, 2024KY252); Hangzhou Agricultural and Social Development Scientific Research Guidance Project (grant number 20220919Y078); and Policy Guidance Project of Major Science and Technology Plan for Social Development of Xiaoshan District (grant number 2021309, 2022327, 2022334).

Data availability
The datasets generated during and analyzed during the current study are not publicly available due to patient privacy concerns but are available from the corresponding author on reasonable request.

Declarations

Ethics approval and consent to participate
This study was approved by the Institutional Review Board of Zhongshan Hospital, Fudan University (B-2021-128), and the study was conducted in accord with the Helsinki Declaration. Informed consent was waived by the committee owing to the retrospective nature of the study.

Consent for publication
Not applicable.

Competing interests
The authors declare no competing interests.

Author details
[1]Department of Radiology, The Second Affiliated Hospital, Zhejiang University School of Medicine, Hangzhou, China
[2]Department of Radiology, The First People's Hospital of Xiaoshan District, Xiaoshan Affiliated Hospital of Wenzhou Medical University, Hangzhou, Zhejiang, China
[3]Department of Research and Development, Chengdu United Imaging Intelligence Co., Ltd., Chengdu, Sichuan, China
[4]Department of Radiology, Zhongshan Hospital, Fudan University, Shanghai, China

Received: 27 November 2024 / Accepted: 19 June 2025
Published online: 01 July 2025

References

1. Sung H, Ferlay J, Siegel RL, Laversanne M, Soerjomataram I, Jemal A, et al. Global Cancer statistics 2020: GLOBOCAN estimates of incidence and mortality worldwide for 36 cancers in 185 countries. CA Cancer J Clin. 2021;71(3):209–49.
2. Leiter A, Veluswamy RR, Wisnivesky JP. The global burden of lung cancer: current status and future trends. Nat Rev Clin Oncol. 2023;20(9):624–39.
3. Howington JA, Blum MG, Chang AC, Balekian AA, Murthy SC. Treatment of stage I and II non-small cell lung cancer: diagnosis and management of lung cancer, 3rd ed: American college of chest physicians evidence-based clinical practice guidelines. Chest. 2013;143(5 Suppl):eS278–313.
4. Silvestri GA, Gonzalez AV, Jantz MA, Margolis ML, Gould MK, Tanoue LT, et al. Methods for staging non-small cell lung cancer: diagnosis and management of lung cancer, 3rd ed: American college of chest physicians evidence-based clinical practice guidelines. Chest. 2013;143(5 Suppl):eS211–50.
5. Saji H, Okada M, Tsuboi M, Nakajima R, Suzuki K, Aokage K, et al. Segmentectomy versus lobectomy in small-sized peripheral non-small-cell lung cancer (JCOG0802/WJOG4607L): a multicentre, open-label, phase 3, randomised, controlled, non-inferiority trial. Lancet. 2022;399(10335):1607–17.
6. Cao C, Chandrakumar D, Gupta S, Yan TD, Tian DH. Could less be more?-A systematic review and meta-analysis of sublobar resections versus lobectomy for non-small cell lung cancer according to patient selection. Lung Cancer. 2015;89(2):121–32.
7. Chae M, Jeon JH, Chung JH, Lee SY, Hwang WJ, Jung W, et al. Prognostic significance of tumor spread through air spaces in patients with stage IA part-solid lung adenocarcinoma after sublobar resection. Lung Cancer. 2021;152:21–6.
8. Jones GD, Brandt WS, Shen R, Sanchez-Vega F, Tan KS, Martin A, et al. A Genomic-Pathologic annotated risk model to predict recurrence in Early-Stage lung adenocarcinoma. JAMA Surg. 2021;156(2):e205601.
9. Li Z, Li F, Pan C, He Z, Pan X, Zhu Q, et al. Tumor cell proliferation (Ki-67) expression and its prognostic significance in histological subtypes of lung adenocarcinoma. Lung Cancer. 2021;154:69–75.
10. Shih AR, Mino-Kenudson M. Updates on spread through air spaces (STAS) in lung cancer. Histopathology. 2020;77(2):173–80.
11. Travis WD, Brambilla E, Nicholson AG, Yatabe Y, Austin JHM, Beasley MB, et al. The 2015 world health organization classification of lung tumors: impact of genetic, clinical and radiologic advances since the 2004 classification. J Thorac Oncol. 2015;10(9):1243–60.
12. Yim J, Zhu LC, Chiriboga L, Watson HN, Goldberg JD, Moreira AL. Histologic features are important prognostic indicators in early stages lung adenocarcinomas. Mod Pathol. 2007;20(2):233–41.
13. Cheng X, Zheng D, Li Y, Li H, Sun Y, Xiang J, et al. Tumor histology predicts mediastinal nodal status and May be used to guide limited lymphadenectomy in patients with clinical stage I non-small cell lung cancer. J Thorac Cardiovasc Surg. 2018;155(6):2648–e562.
14. Kadota K, Nitadori JI, Sima CS, Ujiie H, Rizk NP, Jones DR, et al. Tumor spread through air spaces is an important pattern of invasion and impacts the frequency and location of recurrences after limited resection for small stage I lung adenocarcinomas. J Thorac Oncol. 2015;10(5):806–14.
15. Koike T, Koike T, Yoshiya K, Tsuchida M, Toyabe S. Risk factor analysis of locoregional recurrence after sublobar resection in patients with clinical stage IA non-small cell lung cancer. J Thorac Cardiovasc Surg. 2013;146(2):372–8.
16. Nitadori J, Bograd AJ, Kadota K, Sima CS, Rizk NP, Morales EA, et al. Impact of micropapillary histologic subtype in selecting limited resection vs lobectomy for lung adenocarcinoma of 2 cm or smaller. J Natl Cancer Inst. 2013;105(16):1212–20.
17. Yang X, Sun F, Chen L, Shi M, Shi Y, Lin Z, et al. Prognostic value of visceral pleural invasion in non-small cell lung cancer: A propensity score matching study based on the SEER registry. J Surg Oncol. 2017;116(3):398–406.
18. Chansky K, Sculier JP, Crowley JJ, Giroux D, Van Meerbeeck J, Goldstraw P. The international association for the study of lung Cancer staging project: prognostic factors and pathologic TNM stage in surgically managed non-small cell lung cancer. J Thorac Oncol. 2009;4(7):792–801.
19. Caso R, Sanchez-Vega F, Tan KS, Mastrogiacomo B, Zhou J, Jones GD, et al. The underlying tumor genomics of predominant histologic subtypes in lung adenocarcinoma. J Thorac Oncol. 2020;15(12):1844–56.
20. Dai C, Xie H, Su H, She Y, Zhu E, Fan Z, et al. Tumor spread through air spaces affects the recurrence and overall survival in patients with lung adenocarcinoma > 2 to 3 cm. J Thorac Oncol. 2017;12(7):1052–60.
21. Ost D, Goldberg J, Rolnitzky L, Rom WN. Survival after surgery in stage IA and IB non-small cell lung cancer. Am J Respir Crit Care Med. 2008;177(5):516–23.
22. Zhang J, Wu J, Tan Q, Zhu L, Gao W. Why do pathological stage IA lung adenocarcinomas vary from prognosis? A clinicopathologic study of 176

patients with pathological stage IA lung adenocarcinoma based on the IASLC/ATS/ERS classification. J Thorac Oncol. 2013;8(9):1196–202.
23. Aerts HJ, Velazquez ER, Leijenaar RT, Parmar C, Grossmann P, Carvalho S, et al. Decoding tumour phenotype by noninvasive imaging using a quantitative radiomics approach. Nat Commun. 2014;5:4006.
24. Zwanenburg A, Vallières M, Abdalah MA, Aerts H, Andrearczyk V, Apte A, et al. The image biomarker standardization initiative: standardized quantitative radiomics for High-Throughput image-based phenotyping. Radiology. 2020;295(2):328–38.
25. Gillies RJ, Kinahan PE, Hricak H. Radiomics: images are more than pictures, they are data. Radiology. 2016;278(2):563–77.
26. Lambin P, Leijenaar RTH, Deist TM, Peerlings J, de Jong EEC, van Timmeren J, et al. Radiomics: the Bridge between medical imaging and personalized medicine. Nat Rev Clin Oncol. 2017;14(12):749–62.
27. Limkin EJ, Sun R, Dercle L, Zacharaki EI, Robert C, Reuzé S, et al. Promises and challenges for the implementation of computational medical imaging (radiomics) in oncology. Ann Oncol. 2017;28(6):1191–206.
28. Wu J, Cui Y, Sun X, Cao G, Li B, Ikeda DM, et al. Unsupervised clustering of quantitative image phenotypes reveals breast Cancer subtypes with distinct prognoses and molecular pathways. Clin Cancer Res. 2017;23(13):3334–42.
29. Itakura H, Achrol AS, Mitchell LA, Loya JJ, Liu T, Westbroek EM, et al. Magnetic resonance image features identify glioblastoma phenotypic subtypes with distinct molecular pathway activities. Sci Transl Med. 2015;7(303):303ra138.
30. Lin P, Lin YQ, Gao RZ, Wen R, Qin H, He Y, et al. Radiomic profiling of clear cell renal cell carcinoma reveals subtypes with distinct prognoses and molecular pathways. Transl Oncol. 2021;14(7):101078.
31. Wu FZ, Wu YJ, Tang EK. An integrated nomogram combined semantic-radiomic features to predict invasive pulmonary adenocarcinomas in subjects with persistent subsolid nodules. Quant Imaging Med Surg. 2023;13(2):654–68.
32. Tang EK, Wu YJ, Chen CS, Wu FZ. Prediction of the stage shift growth of early-stage lung adenocarcinomas by volume-doubling time. Quant Imaging Med Surg. 2024;14(6):3983–96.
33. Dong H, Yin LK, Qiu YG, Wang XB, Yang JJ, Lou CC, et al. Prediction of high-grade patterns of stage IA lung invasive adenocarcinoma based on high-resolution CT features: a bicentric study. Eur Radiol. 2023;33(6):3931–40.
34. Dong H, Xi Y, Liu K, Chen L, Li Y, Pan X, et al. A Radiological-Radiomics model for differentiation between minimally invasive adenocarcinoma and invasive adenocarcinoma less than or equal to 3 cm: A two-center retrospective study. Eur J Radiol. 2024;176:111532.
35. Perez-Johnston R, Araujo-Filho JA, Connolly JG, Caso R, Whiting K, Tan KS, et al. CT-based radiogenomic analysis of clinical stage I lung adenocarcinoma with histopathologic features and oncologic outcomes. Radiology. 2022;303(3):664–72.
36. Detterbeck FC, Boffa DJ, Kim AW, Tanoue LT. The eighth edition lung Cancer stage classification. Chest. 2017;151(1):193–203.
37. Chen L, Gu D, Chen Y, Shao Y, Cao X, Liu G, et al. An artificial-intelligence lung imaging analysis system (ALIAS) for population-based nodule computing in CT scans. Comput Med Imaging Graphics: Official J Comput Med Imaging Soc. 2021;89:101899.
38. Nicholson AG, Tsao MS, Beasley MB, Borczuk AC, Brambilla E, Cooper WA, et al. The 2021 WHO classification of lung tumors: impact of advances since 2015. J Thorac Oncol. 2022;17(3):362–87.
39. Rusch VW, Asamura H, Watanabe H, Giroux DJ, Rami-Porta R, Goldstraw P. The IASLC lung cancer staging project: a proposal for a new international lymph node map in the forthcoming seventh edition of the TNM classification for lung cancer. J Thorac Oncol. 2009;4(5):568–77.
40. Yoshizawa A, Sumiyoshi S, Sonobe M, Kobayashi M, Fujimoto M, Kawakami F, et al. Validation of the IASLC/ATS/ERS lung adenocarcinoma classification for prognosis and association with EGFR and KRAS gene mutations: analysis of 440 Japanese patients. J Thorac Oncol. 2013;8(1):52–61.
41. Okudela K, Woo T, Saigusa Y, Arai H, Matsumura M, Mitsui H, et al. A method to obtain reproducible Ki-67 indices in lung adenocarcinoma. Histopathology. 2021;78(3):414–23.
42. Pan Y, Zhang Y, Ye T, Zhao Y, Gao Z, Yuan H, et al. Detection of novel NRG1, EGFR, and MET fusions in lung adenocarcinomas in the Chinese population. J Thorac Oncol. 2019;14(11):2003–8.
43. Shimada Y, Saji H, Yoshida K, Kakihana M, Honda H, Nomura M, et al. Pathological vascular invasion and tumor differentiation predict cancer recurrence in stage IA non-small-cell lung cancer after complete surgical resection. J Thorac Oncol. 2012;7(8):1263–70.
44. Zhang Y, Sun Y, Xiang J, Zhang Y, Hu H, Chen H. A clinicopathologic prediction model for postoperative recurrence in stage Ia non-small cell lung cancer. J Thorac Cardiovasc Surg. 2014;148(4):1193–9.
45. Wang S, Zhang B, Qian J, Qiao R, Xu J, Zhang L, et al. Proposal on incorporating lymphovascular invasion as a T-descriptor for stage I lung cancer. Lung Cancer. 2018;125:245–52.
46. Ikeda T, Kadota K, Go T, Misaki N, Haba R, Yokomise H. Segmentectomy provides comparable outcomes to lobectomy for stage IA Non-small cell lung Cancer with spread through air spaces. Semin Thorac Cardiovasc Surg. 2023;35(1):156–63.
47. Bao J, Liu Y, Ping X, Zha X, Hu S, Hu C. Preoperative Ki-67 proliferation index prediction with a radiomics nomogram in stage T1a-b lung adenocarcinoma. Eur J Radiol. 2022;155:110437.
48. Chen LW, Yang SM, Wang HJ, Chen YC, Lin MW, Hsieh MS, et al. Prediction of micropapillary and solid pattern in lung adenocarcinoma using radiomic values extracted from near-pure histopathological subtypes. Eur Radiol. 2021;31(7):5127–38.
49. Wang X, Zhao X, Li Q, Xia W, Peng Z, Zhang R, et al. Can peritumoral radiomics increase the efficiency of the prediction for lymph node metastasis in clinical stage T1 lung adenocarcinoma on CT? Eur Radiol. 2019;29(11):6049–58.
50. Zha X, Liu Y, Ping X, Bao J, Wu Q, Hu S, et al. A nomogram combined radiomics and clinical features as imaging biomarkers for prediction of visceral pleural invasion in lung adenocarcinoma. Front Oncol. 2022;12:876264.
51. Zhang Z, Liu Z, Feng H, Xiao F, Shao W, Liang C, et al. Predictive value of radiological features on spread through air space in stage cIA lung adenocarcinoma. J Thorac Dis. 2020;12(11):6494–504.
52. Andreassen CN, Schack LM, Laursen LV, Alsner J. Radiogenomics - current status, challenges and future directions. Cancer Lett. 2016;382(1):127–36.
53. Liang W, Cai K, Chen C, Chen H, Fang W, Fu J, et al. Society for translational medicine consensus on postoperative management of EGFR-mutant lung cancer (2019 edition). Transl Lung Cancer Res. 2019;8(6):1163–73.
54. Izar B, Sequist L, Lee M, Muzikansky A, Heist R, Iafrate J, et al. The impact of EGFR mutation status on outcomes in patients with resected stage I non-small cell lung cancers. Ann Thorac Surg. 2013;96(3):962–8.
55. Takamochi K, Oh S, Matsunaga T, Suzuki K. Prognostic impacts of EGFR mutation status and subtype in patients with surgically resected lung adenocarcinoma. J Thorac Cardiovasc Surg. 2017;154(5):1768–e741.
56. Yang F, Sun K, Li F, Li X, Shi J, Sun X et al. The prognostic impact of epidermal growth factor receptor mutation in clinical stage I lung adenocarcinoma. Ann Thorac Surg. 2023.
57. Diao WY, Ding CL, Yuan BY, Li Z, Sun N, Huang JB. Clinical characteristics and prognosis of HER2 gene phenotype in patients with Non-Small cell lung Cancer. Int J Gen Med. 2021;14:9153–61.
58. Toh CK, Ahmad B, Soong R, Chuah KL, Tan SH, Hee SW, et al. Correlation between epidermal growth factor receptor mutations and expression of female hormone receptors in East-Asian lung adenocarcinomas. J Thorac Oncol. 2010;5(1):17–22.
59. Mazières J, Peters S, Lepage B, Cortot AB, Barlesi F, Beau-Faller M, et al. Lung cancer that harbors an HER2 mutation: epidemiologic characteristics and therapeutic perspectives. J Clin Oncol. 2013;31(16):1997–2003.

Publisher's note